PHYSICAL CHEMISTRY CHEMICAL PHYSICS (ISSN: 1463-9076) (eISSN: 1463-9084)
16: (34) pp. 18533-18544. (2014)

DOI: 10.1039/C4CP01832J

Competitive Reaction Pathways in Vibrationally Induced Photodissociation of H_2SO_4

Juvenal Yosa Reyes,[a‡] Tibor Nagy,[a‡] and Markus Meuwly*[a]

Received Xth XXXXXXXXXX 20XX, Accepted Xth XXXXXXXXX 20XX
First published on the web Xth XXXXXXXXXX 200X
DOI: 10.1039/b000000x

Vibrationally induced photodissociation of sulfuric acid into H_2O + SO_3 is investigated based on reactive molecular dynamics (MD) simulations. Multisurface adiabatic reactive MD simulations allow to follow both, H-transfer and water elimination after excitation of the ν_9 OH-stretching mode. Analysis of several thousand trajectories finds that the H_2O and SO_3 fragments have distinct final state distributions with respect to translational, rotational, and vibrational degrees of freedom. Rotational distributions peak at quantum numbers $j \leq 5$ for water and $j \approx 60$ for SO_3. The final state distributions should be useful in identifying products in forthcoming experiments. Based on the MD trajectories, a kinetic scheme is developed which is able to explain most of the trajectory data and suggests that IVR is very rapid. Typical lifetimes of the excited complex range from several 10 picoseconds to hundreds of nanoseconds, depending on the excitation level. Including temperature and pressure profiles characteristic for the stratosphere in the kinetic model lead show that excitations higher than $\nu_9 = 4$ can significantly contribute to the photolysis rate. This extends and specifies earlier work in that multi-level modeling is required to understand the significance of vibrationally induced decomposition pathways of sulfuric acid in the middle atmosphere.

1 Introduction

The chemistry of sulfur-containing compounds is of great importance in atmospheric sciences. Sulfur is mainly emitted in the form of dimethyl sulfide (DMS)[1–3] and sulfur dioxide (SO_2)[4,5]. One of the main intermediates formed from the oxidation of DMS is SO_2[6,7] which is subsequently oxidized to sulfur trioxide (SO_3) by reaction with the hydroxyl radical ($HO^{\cdot}$) and with O_2.[8–10] Subsequently, SO_3 is hydrated to sulfuric acid (H_2SO_4) and sulfates (SO_4^{2-}). These reactions have been extensively studied, mainly because of their importance in tropospheric aerosol layer formation, which is related to global atmospheric chemistry[11] including cloud condensation,[12] altering the chemical composition and influencing the course of aqueous reactions in clouds. On the other hand, the anomalous enhancement of SO_2 in the polar stratospheric aerosol layer during springtime has been postulated to originate from photodissociation of H_2SO_4 to form water and sulfur trioxide which rapidly decays to SO_2.[13] This photodissociation process was previously assumed to take place *via* absorption of ultraviolet (UV) radiation. However, the electronic absorption spectrum of H_2SO_4 above 140 nm could not be found experimentally[14–16] or in computations.[17–19] The lowest energy electronic transition in H_2SO_4, using coupled cluster methods and correlation consistent basis sets, was calculated to be at 139 nm.[20] This lead to the conclusion that H_2SO_4 absorbs in the IR and NIR regions, with the OH stretching vibration playing the dominant role, and that the electronic excitation will only be significant at very high energies, well above those available from the sun in the earths atmosphere.[15] Because UV photons are absorbed at higher altitudes only a small fraction of photons with wavelengths shorter than 179 nm will penetrate into the lower mesosphere and upper stratosphere,[21] making UV photodissociation of H_2SO_4 unlikely to occur at lower altitudes.[14]

Following this, it was proposed that some OH-containing species in the atmosphere absorb visible radiation which can potentially induce transitions to vibrational overtones with several quanta in the ν_9 OH stretch mode.[22,23] The vibrational overtones for H_2SO_4 were previously calculated[16] and found to be in the visible range, at 741 nm, 608 nm, and 519 nm wavelength, for excitations of $\nu_9 = 4$, 5, and 6. Also, the computed absorption cross sections at the QCISD/6-311++G(2d,2p) level of theory were found to be appreciable for these vibrational levels, ranging from $2.0 \cdot 10^{-21}$ to $2.6 \cdot 10^{-23}$ cm molecule^{-1}. Depending on the altitude, the reported first order photodissociation rate constants J are 10^{-8} s^{-1} (vibrational overtones) and 10^{-11} to 10^{-8} s^{-1} (UV excitation), respectively. Related calculations suggest that dissociation of H_2SO_4 is possible mainly from highly excited

† Electronic Supplementary Information (ESI) available: [details of any supplementary information available should be included here]. See DOI: 10.1039/b000000x/

[a] *Address, Klingelbergstrasse 80, Basel, Switzerland. Fax: +41 (0)61 267 38 55; Tel: +41 (0)61 267 38 21; E-mail: m.meuwly-at-unibas.ch*

‡ These authors contributed equally to this work

OH-stretching vibrational overtones.[16] Hence, the vibrational spectroscopy of H_2SO_4 has been studied intensely in the near-infrared and visible regions, both experimentally[14,24–27] and computationally.[18,19,27] Even though the vibrationally induced decomposition $H_2SO_4 \rightarrow SO_3$+H_2O has not been observed, it is conceivable that exciting higher OH-stretching states in H_2SO_4 by visible light provides sufficient energy for photodissociation. This process is likely because the energy barrier for dissociation is in the range of 32-40 kcal/mol, according to calculations.[28–30] On the other hand, vibrational mode-specific reactivity has already been observed experimentally, for example for the reaction of methane on a nickel surface.[31]

Previously, the dynamics of the photodissociation reaction following excitation with $v_9 = 4$ to 6 quanta in the OH-stretching vibration has been investigated by classical trajectory simulations together with semiempirical PM3 electronic structure calculations,[32] or parametrized force fields (FFs).[30] It was found that the photodissociation reaction occurs typically on a picosecond timescale - depending on the level of excitation - which is significantly faster than the collision rate in the atmosphere.[33] The molecular dynamics (MD) simulations also showed that photoexcitation can lead to a) intramolecular H-transfer or b) nonstatistical, impulsive H_2O-elimination and statistical, intramolecular vibrational-energy redistribution (IVR).[30,32]

Because vibrationally induced photodissociation has as yet not been observed experimentally for H_2SO_4, suitable observables are required to detect such a decay mechanism. One possibility is to determine final state distributions of the individual energy components for the fragments H_2O and SO_3 after photodissociation. Such information is now available from suitable experiments.[34–36] Also a competition between the two reaction channels, which have similar activation energies, may affect the decay rate. In order to understand in detail the dynamics of vibrationally induced decomposition of H_2SO_4, reactive molecular dynamics simulations are performed using multisurface adiabatic reaction dynamics (MS-ARMD).[37] This method a) combines fitted empirical force fields for different user-defined states to a global potential energy surface (PES) of the system, b) is based on adiabatic reactive MD[38,39], c) is capable of treating multiple reaction pathways and d) conserves total energy along a reactive trajectory. As MS-ARMD is a force field-based method, a statistically significant number of trajectories can be run and analyzed. In the present work we investigate the dynamics on a new, fully dimensional reactive PES capable of following intramolecular H-transfer and water elimination in H_2SO_4. This provides lower bounds for reaction rates and the information to analyze the reaction products' energetics including translational, rotational and vibrational contributions which will eventually be relevant for comparison with experiments.

2 Computational Methods

2.1 Force Field Parametrization

The present work employs a global, parametrized and reactive potential energy surface (PES) to follow intramolecular H-transfer and water elimination ($H_2SO_4 \rightarrow H_2O$+SO_3) in H_2SO_4 upon vibrational excitation of the OH-stretching mode. For this, MS-ARMD was employed.[37] The global PES is based on reference electronic structure calculations at the MP2/6-311G++(2d,2p) level. All *ab initio* calculation were performed with Gaussian09.[40] The energy at the equilibrium geometry of H_2SO_4 was chosen as the global zero and serves as a common origin for all *ab initio* energies. Using previously and separately parametrized FFs for the different states, including H_2O, SO_3, the $H_2O\cdots SO_3$ van der Waals complex, and H_2SO_4, representative geometries were collected from MD simulations which cover the regions of the multidimensional PES relevant to the equilibrium dynamics.[30] Starting from the optimized geometry, each system was heated to 300 K, and subsequently equilibrated for 40 ps, followed by 10 ns of free dynamics at constant total energy. Along the three trajectories, approximately 1000 geometries were selected for H_2O, SO_3 and H_2SO_4, respectively. A similar procedure was followed for the $H_2O\cdots SO_3$ van der Waals complex (see below). Additionally, a rigid 2D scan along the dihedral angles H6-O7-S1-O4 and H5-O4-S1-O6 (Figure 1) in H_2SO_4 was performed resulting in an extra 1296 reference data points (648 independent calculations) which were added to the previous 3000 structures.

The functional form of the force field which describes the H_2SO_4 and H_2O+SO_3 states, including the $H_2O\cdots SO_3$ van der Waals complex, is

$$\begin{aligned} V(\mathbf{x}) = & \sum_{\text{bonds}} D_e(1-e^{-\beta(r-r_0)})^2 + \sum_{\text{angles}} K_\theta(\theta-\theta_0)^2 \\ & + \sum_{\text{Urey-Bradley}} K_{\text{UB}}(S-S_0)^2 \sum_{\text{dihedral}} H_\phi(1+\cos(n\phi-\delta)) \\ & + \sum_{\text{impropers}} K_\omega(\omega-\omega_0)^2 \\ & + \sum_{ij}\left\{\frac{n\varepsilon_{ij}}{m-n}\left[\left(\frac{r_{\min,ij}}{r_{ij}}\right)^m - \frac{m}{n}\left(\frac{r_{\min,ij}}{r_{ij}}\right)^n\right] + \frac{q_i q_j}{4\pi\varepsilon_0 r_{ij}}\right\} \end{aligned} \quad (1)$$

where r_0 is the equilibrium bond distance, D_e is the dissociation energy, and β controls the steepness and width of the Morse potential. In all FFs the bonds were treated with Morse potentials. For every angle in the three molecules H_2SO_4,

H_2O and SO_3 (i.e., H5-O4-S1, O2=S1=O3, etc., see Figure 1) two potentials were used; one of them is the usual harmonic potential involving three atoms, whereas the second is a Urey-Bradley term which is a quadratic interaction potential of the distance between atoms separated by two bonds (1,3 interaction). All dihedral angles in H_2SO_4 are described by proper dihedral terms. For SO_3 additional improper dihedral potentials were employed symmetrically to maintain its planarity. Generalized-exponent Lennard-Jones potentials (or Mie potentials)[41] were used for the H_2SO_4 molecule between 1-4 (e.g. H5 and O2 see Figure 1) and 1-5 (between H5 and H7 see Figure 1) neighboring atoms. Point charges were obtained by fitting the molecular electrostatic potential (ESP) using the CHELPG scheme within Gaussian09.[42] Initial values for all other parameters were taken or calculated (i.e. for generalized Lennard-Jones) from standard CHARMM parameters[43] and a standalone Fortran code based on the downhill simplex algorithm[44] was used for optimizing the parameters to match the *ab initio* reference energies.

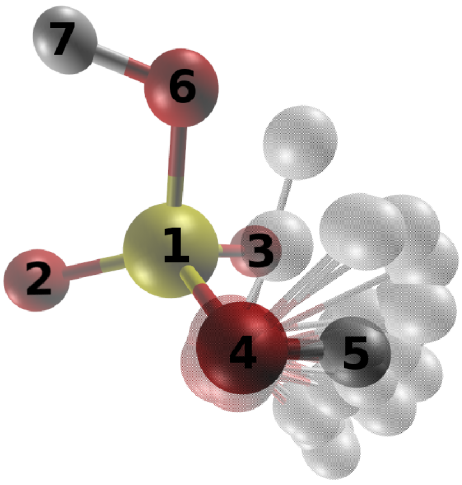

Fig. 1 Yosa et al.: Sulfuric acid with atom numbering used throughout the text. The librational motion of O4 and H5, related to the dihedral angle H5-O4-S1-O6, is indicated by light spheres.

With the refined FF parameters for H_2O and SO_3, the generalized Lennard-Jones (GLJ) parameters and atomic charges (last term in Eq. 2) were fitted in order to describe the intermolecular interactions for the $H_2O\cdots SO_3$ van der Waals complex. Initial guesses for the GLJ parameters are obtained from the Lennard-Jones parameters between pairs of atoms i and j using the Lorentz-Berthelot combination rules in which ε_{ij} is the geometric mean of ε_i and ε_j and $r_{\min,ij}$ is the arithmetic mean of $r_{\min,i}$ and $r_{\min,j}$. For the GLJ potential, ε_{ij} (>0) and $r_{\min,ij}$ are also the well-depth and the corresponding separation at this energy minimum, respectively. As a reference for the fitting, electronic structure calculations were carried out on approximately 1000 geometries collected from an MD simulation at 300 K for the van der Waals complex (see above). Two different parameter sets describe the reactant and product.

The FF in Eq. 2 is also suitable to follow H-transfer in sulfuric acid. Because there are 12 different ways how the two H-atoms can be arranged, the final PES needs to be permutationally invariant. In total, there exist 4 different final states which give rise to 16 FFs that are required to describe all possible reaction pathways of interest in the present work. The 16 states are connected through 48 transition states.[37]

In a next step, the FFs for the states involved in the reactions (H_2SO_4, and H_2O+SO_3) are combined to a global PES for reactive molecular dynamics simulations. For this, geometrically dependent weights $w_i(\mathbf{x})$ are used to generate the global PES from the individual FFs $V_i(\mathbf{x})$.[37] Increased flexibility for the MS-ARMD PES is required in the barrier regions where the FFs of the states - i.e. H_2SO_4 and H_2O+SO_3 - cross. This is accomplished by using products of Gaussian and polynomial functions (GAPOs) of the energy difference (ΔV_{ij}) between the PESs involved[37]

$$\Delta V^{ij}_{\mathrm{GAPO},k}(\mathbf{x}) = \exp\left(-\frac{\left(\Delta V_{ij}(\mathbf{x}) - V^0_{ij,k}\right)^2}{2\sigma^2_{ij,k}}\right) \times \sum_{l=0}^{m_{ij,k}} a_{ij,kl}\left(\Delta V_{ij}(\mathbf{x}) - V^0_{ij,k}\right)^l. \quad (2)$$

where $V^0_{ij,k}$ and $\sigma_{ij,k}$ denote the center and the standard deviation of the Gaussian functions, respectively, $\Delta V_{ij}(\mathbf{x}) = V_i(\mathbf{x}) - V_j(\mathbf{x})$, and $a_{ij,kl}$ are the coefficients of the polynomials. The global PES is then a weighted sum of PESs (first term in Eq. 3) combined with the weighted GAPOs (second term in Eq. 3) which allows to better capture the barrier region

$$V_{\text{MS-ARMD}}(\mathbf{x}) = \sum_{i=1}^{n} w_i(\mathbf{x}) V_i(\mathbf{x}) + \sum_{i=1}^{n-1}\sum_{j=i+1}^{n}\left[w_i(\mathbf{x}) + w_j(\mathbf{x})\right]\sum_{k=1}^{n_{ij}} \Delta V^{ij}_{\mathrm{GAPO},k}(\mathbf{x}) \quad (3)$$

and the sum runs up to $n = 16$. Parameters of the GAPO functions were optimized to reproduce the barrier height for both processes of interest, water elimination and intramolecular H-transfer. The reference points in the fit were augmented by points along both minimum energy paths (MEPs) determined

from quadratic synchronous transit (QST2) calculations[45] followed by an intrinsic reaction coordinate (IRC) calculation at the MP2/6-311G++(2d,2p) level of theory. The MS-ARMD switching parameter ΔV and the overall shifts of the FFs (see ref.[37] for definitions) were optimized with the downhill simplex algorithm using $k = 3$ GAPOs with $m_{ij,k} = 1$ (first order polynomial) for H_2O elimination, and $k = 2$ GAPOs with $m_{ij,k} = 2$ for the H-transfer reaction.[37]

The energy profile along the reference minimum energy path can be reproduced very closely (RMSD = 0.55 kcal/mol), as is shown in Figure 2A (red squares) whereas the remaining electronic structure data are somewhat further away from a 1:1 correlation, but still close to it. Figure 2B illustrates the two minimum energy pathways for water elimination and intramolecular H-transfer. The reference *ab initio* calculations yield a barrier height of 32.0 kcal/mol for water elimination, and 36.6 kcal/mol for intramolecular H-transfer, which is also closely captured by the fitted PES. The energetics establishes that for a meaningful treatment of the reactive dynamics both pathways need to be included. The present barrier for water elimination compares with previous estimates ranging from 32 to 40 kcal/mol depending on the level of theory used.[28–30]

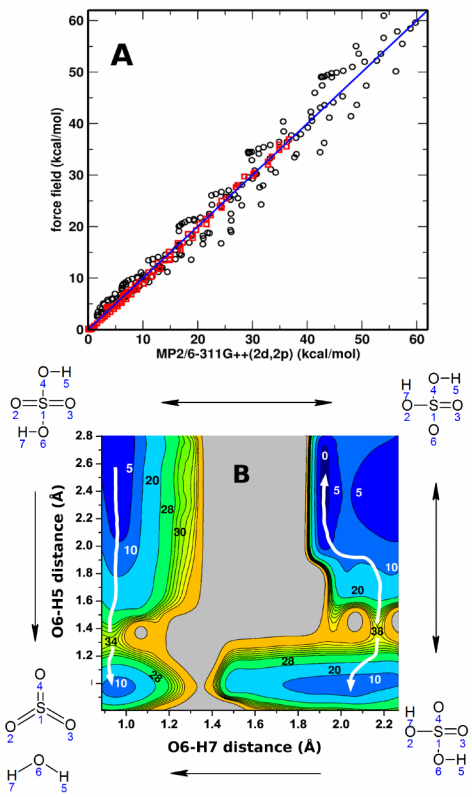

Fig. 2 Yosa et al.: Panel A shows the quality of the fitted PES relative to the *ab initio* reference energies. Points along the MEPs (red squares) and remaining reference points (black circles) are distinguished. Panel B shows the fully relaxed MS-ARMD PES for both, intramolecular H-transfer and water elimination, in the space defined by distances O6-H5 and O6-H7. The white lines indicate approximate MEPs for the two possible reactions, water elimination (left-hand side) and H-transfer (right-hand side). Selected isocontours (in kcal/mol) are labelled.

2.2 Molecular Dynamics Simulations

All MD simulations were carried out with CHARMM[46] with provisions for bond-breaking and bond-formation through MS-ARMD.[37] Starting from a geometry optimized structure of H_2SO_4, the system was heated to 300 K. The equations of motion were solved with the leapfrog Verlet algorithm with a time step of $\Delta t = 0.1$ fs during 40 ps and equilibrated for 40 ps, followed by 50 ps of free dynamics simulations (i.e. constant energy). The small time step is required to appropriately follow the rapid dynamics of the H-atoms.

Vibrational excitation of the OH stretching mode was modelled by scaling the instantaneous velocities along the ν_9 normal mode which is predominantly an OH-stretching mode and highly localized. The OH stretch potential can be realistically described by a Morse potential, for which the exact energy levels are known. The excitation energies include 13490 cm^{-1} (38.6 kcal/mol, $\nu_9 = 4$), 16494 cm^{-1} (47.2 kcal/mol, $\nu_9 = 5$), and 19328 cm^{-1} (55.3 kcal/mol, $\nu_9 = 6$). Such an approach has also been successfully used for studying proton transfer in H-bonded complexes.[47] Alternatively, positions and velocities can be scaled whereby both the kinetic and potential energies are modified.[48] One possible drawback of modifying both positions and momenta is the fact that, after excitation, a short equilibration period (a few picoseconds) is required to avoid artifacts due to close proximity of atoms.

2.3 Final State Analysis

For the final state analysis, the total energy of the system was decomposed into translational, rotational and vibrational components of each fragment. The translational energy of a reaction product is $E_{\text{trans}} = \frac{1}{2} M v_{\text{CM}}^2$ where M and v_{CM} denote the mass and the velocity of the center of mass for the given fragment (H_2O and SO_3). Following classical mechanics, the angular momentum vector of a reaction product (with N atoms) is $\mathbf{L} = \sum_{i=1}^{N} m_i (\mathbf{r}_i - \mathbf{r}_{\text{CM}}) \times (\mathbf{v}_i - \mathbf{v}_{\text{CM}})$. Here, $\mathbf{r}_{\text{CM}}$ and $\mathbf{v}_{\text{CM}}$ denote the position and the velocity vectors of the center

of mass for the given fragment. This yields the rotational energy $E_{\mathrm{rot}} = \frac{1}{2}\mathbf{L}^{\mathrm{T}}\Theta^{-1}\mathbf{L}$ where Θ is the moment of inertia tensor of the fragment $\Theta = \sum_{i=1}^{N} m_i \left(\mathbf{E}r_i^2 - \mathbf{r}_i\mathbf{r}_i^{\mathrm{T}}\right)$ and $\mathbf{E}$ is the unit tensor. From E_{trans} and E_{rot} the vibrational energy of each product is determined through $E_{\mathrm{vib}} = E_{\mathrm{kin}} - E_{\mathrm{trans}} - E_{\mathrm{rot}} + V$ where V denotes the intramolecular potential energy of the given reaction product. Once the two fragments have moved sufficiently far from the interaction region (here taken as 20 Å between the SO_3-sulfur and the H_2O-oxygen atoms), the translational and rovibrational energy of each fragment will be constant. As the vibrational and rotational modes in each fragment keep on exchanging energy if the angular momentum is nonzero, these quantities are averaged over periods much longer (i.e. 5 ps) than the characteristic time for vibrations within the molecules.

The angular momentum quantum number j can be calculated from the classical-quantum correspondence relationship $L^2 = j(j+1)\hbar^2$ in which $\hbar$ is Planck's constant. The orbital angular momentum ($\mathbf{L}_{\mathrm{orbital}}$) can be determined from the individual angular momenta of the fragments and from the conservation of total angular momentum. Considering the photodissociation reaction as an inverse scattering process in the framework of classical mechanics, it is useful to introduce the perpendicular distance (b_{scatter}) between the asymptotic paths of the fragments in analogy with the impact parameter of bimolecular reactions: $b_{\mathrm{scatter}} = L_{\mathrm{orbital}}/\sqrt{2\mu E_{\mathrm{trans,tot}}}$. Here, μ and $E_{\mathrm{trans,tot}}$ are the reduced mass and the sum of translational energies of the fragments, respectively, and $L_{\mathrm{orbital}} = |\mathbf{L}_{\mathrm{orbital}}|$. This scattering parameter provides information about the relative displacements of the fragmentation partners at the moment of breakup.

3 Results

3.1 Validation of the Force Field

The energy-minimized structures at the MP2/6-311G++(2d,2p) level and using the force field has C_2-symmetry (see Figure 1).[49] A comparison of equilibrium bond lengths, angles and dihedral angles between the two treatments is provided in Table S-I (supporting information). The positional root-mean-square deviations (RMSDs) are 0.04 Å for H_2SO_4 and 0.001, 0.001 and 0.13 Å for SO_3, H_2O and the vdW complex, respectively. For bond lengths and valence angles the average difference between the MP2 reference and the FF structures is less than 0.03 Å and around 3°, respectively. This, together with the results from Figure 2A, suggests that the force field is parametrized in a meaningful way.

Previous computational work on rotamers for sulfuric acid revealed the existence of two minimum energy geometries with point group symmetries C_2 and C_s, connected by two saddle points with C_1 symmetry, 4.9 kcal/mol and 5.4 kcal/mol higher in energy than the C_2 structure. The lower of the two saddle points is called C_{1a} whereas the higher one is C_{1b}. The energies of the two saddle points at the current level of theory are around 1 kcal/mol higher than those computed by Lohr and Havey, who found 3.34 and 4.16 kcal/mol (at the HF/STO-3G level) and 1.45 and 4.06 kcal/mol (at the B3LYP/6-311G(2d,2p) level) in the two studies, respectively.[24,50]

A comparison between the reference and fitted FF energies for the torsional degrees of freedom is presented in Figure 3. The two saddle points on the FF PES are 3.7 kcal/mol and 4.3 kcal/mol above the global C_2 minimum which compares with 4.9 kcal/mol and 5.4 kcal/mol in the MP2 reference calculations. In addition, a normal mode analysis was performed in order to compare the experimentally observed vibrational frequencies with those from the MP2 and FF calculations. All MP2 frequencies were scaled with a factor of 0.97 (MP2/6-31+G(d,p)[51] and MP2-fc/6-311G(d,p)[52]). As the FF is based on MP2 calculations, the vibrational frequencies obtained from the normal mode analysis using the FF were also scaled with the same scaling factor. Comparisons of individual frequencies are reported in Table S-II (supporting information). The average differences between experimental,[53–55] MP2 and FF harmonic frequencies for H_2SO_4, SO_3, H_2O and $H_2O\cdots SO_3$ are [72, 20, 22, 41] cm^{-1}(MP2 vs. FF), [53, 52, 87, 65] cm^{-1} (expt. vs. MP2), and [88, 68, 65, 69] cm^{-1} (expt. vs. FF).

3.2 Reaction Dynamics

With a suitably formulated and accurately parametrized FF which can reproduce optimized geometries, torsional and reaction barrier heights, and vibrational frequencies (see Tables S-I and S-II (supporting information) and Figures 2 and 3) close to those computed from reference electronic structure calculations at the MP2 level, reactive molecular dynamics simulations were carried out. For a statistically significant number of reactive events, 7000 independent trajectories were run using MS-ARMD for $\nu_9 = 4$, 5, and 6. The global PES can describe the two energetically accessible channels: water elimination and intramolecular H-transfer. Because the barrier heights for both processes are accurately described by the MS-ARMD PES, the competition between the two reactive channels can also be studied.

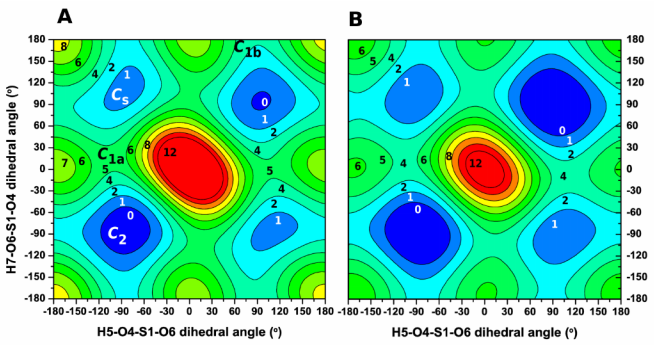

Fig. 3 Yosa et al.: Calculated PES along dihedral angles H5-O4-S1-O6 (ϕ) and H7-O6-S1-O4 (ϕ') at (A) the MP2/6-311G++(2d,2p) level (rigid scan) and (b) with the FF (rigid scan). The two minima are C_2 and C_s which are connected through transition states C_{1a} (4.9 kcal/mol) and C_{1b} (5.4 kcal/mol).

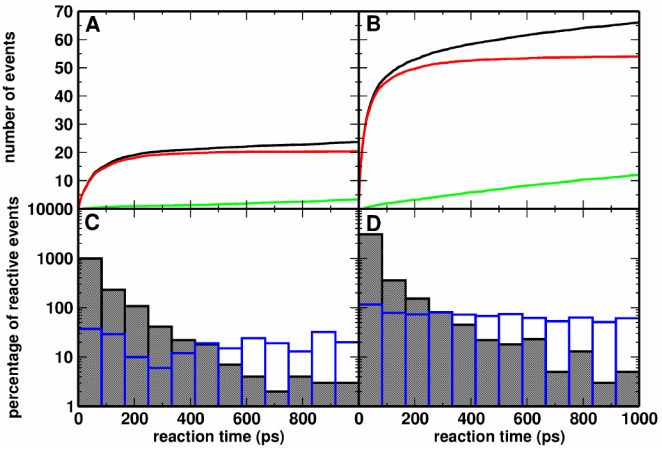

Fig. 4 Yosa et al.: Percentage of water elimination after excitation of $\nu_9 = 5$ (A) and $\nu_9 = 6$ (B). Black, red and green curves correspond to overall, direct water elimination, and water elimination preceded by intramolecular H-transfer, respectively. Panel (C) and (D) reports histograms for the distribution of reaction times for direct water elimination (black) and for water elimination preceded by intramolecular H-transfer (blue). (C) $\nu_9 = 5$ and (D) $\nu_9 = 6$ on a semi-logarithmic scale.

From 7000 independent trajectories with a maximum simulation time of 1 ns, 4048 (57.8%), 5418 (77.4%) and 5599 (79.9%) trajectories for excitation of $\nu_9 = 4$, 5 and 6, respectively, showed either water elimination or intramolecular H-transfer. The remaining trajectories (42.2%, 22.6% and 20.1%) are not reactive. From the reactive trajectories, 57.3% ($\nu_9 = 4$), 52.6% ($\nu_9 = 5$) and 13.8% ($\nu_9 = 6$), exhibit intramolecular H-transfer without subsequent water elimination. For water elimination, two different mechanisms were found: i) water elimination is the only process and ii) intramolecular H-transfer precedes water elimination. For i) 35 (0.5%), 1495 (21.4%) and 3779 (54.0%) trajectories were observed whereas for ii) 0, 236 (3.4%) and 853 (12.2%) events were found for $\nu_9 = 4$, 5 and 6, respectively. These results suggest that excitation of $\nu_9 = 4$ is probably not sufficient to obtain significant amounts of SO_3 on the nanosecond time scale whereas excitation of $\nu_9 \geq 5$ results in rapid decay.

Panels A and B of Figure 4 report the percentage of reactive events as a function of reaction time for water elimination with $\nu_9 = 5$ and 6, respectively. For excitation with $\nu_9 = 5$ a maximum lifetime for direct water elimination of around 300 ps is found which reduces to approximately 100 ps for excitation with $\nu_9 = 6$. Contrary to that, for case ii) the percentage of decays increases linearly for both, excitation of $\nu_9 = 5$ and 6 (green curves in Figure 4).

Figure 4 C shows lifetime distributions for the two possible mechanisms on a semi-logarithmic scale. Direct water elimination (grey) for $\nu_9 = 5$ (top) is slower than that for $\nu_9 = 6$ (bottom) while for the process in which water elimination is preceded by intramolecular H-transfer (blue), the rates are constant in time. However, the absolute number of events differs by a factor of ≈ 5 between the two excitation levels. For excitation of $\nu_9 = 6$ the trajectories in which H_2SO_4 did not decay within 1 ns the dynamics was continued out to 40 ns. By that time 6844 (98 %) out of the 7000 trajectories decayed to H_2O and SO_3 of which 3995 (57 %) went through direct water elimination and the remaining 2849 (40 %) were preceded by intramolecular H-transfer. 150 events (2 %) experienced only intramolecular H-transfer and 6 events (0.08 %) did not exhibit any reaction at all.

For excitation of $\nu_9 = 6$, 90 % of events are found to occur in less than 10 ns (Figure S-I black curve). For direct water elimination, a rapid increment is observed until 400 ps after which very few additional new events are observed. Conversely, water elimination preceded by intramolecular H-transfer continues to increase until ≈ 15 ns after vibrational excitation.

Figure 5 reports time series of selected internal coordinates along two trajectories with very different reaction times for water elimination. The left panels correspond to a rapid reaction occurring in less than 2 ps whereas the right hand panels are for a situation in which the vibrational excitation redistributes on the 100 ps time scale before water elimination. For the rapid process, the H5-O4-S1-O6 dihedral angle at time 0 starts close to the C_2 minimum (90°). Initially, the motion of this dihedral angle is similar to a librational mode,

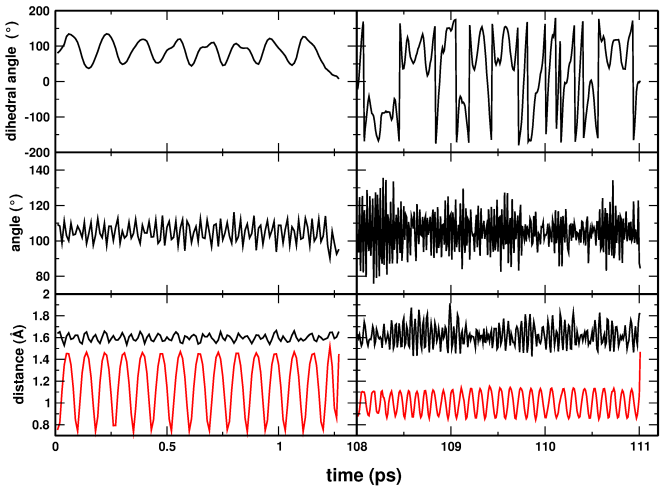

Fig. 5 Yosa et al.: Time series of selected internal coordinates for H_2SO_4, including the H5-O4-S1-O6 dihedral angle (top), the H5-O4-S1 angle (middle), and the H5-O4 (red curve) and S1-O6 (black curve) bonds (bottom). Left column reports the data for a rapid water elimination reaction (breakup after 1.26 ps) whereas the right column corresponds to the last 3 ps of a slow reaction (breakup after ≈ 111 ps), for two representative trajectories with excitation of $\nu_9 = 6$. Note the characteristic torsional dynamics in the left panel.

fluctuating around 80°. When the reaction occurs at around 1.26 ps, the H5-O4-S1-O6 dihedral angle reaches 0°, which is the lowest saddle point in the transition from the C_2 to the C_s minimum (see Figure 1 and 3). On the other hand, the H5-O4 bond length fluctuates around an average value of about 1.1 Å and reaches a maximum of 1.45 Å when the reaction takes place at 1.26 ps. At this point, the distance between atoms H5 and O6 is ≈ 1.4 Å which is close to the transition state geometry, see Figure 1.[28–30] Figure 5 suggests that for trajectories with such a rapid reaction, these two coordinates (dihedral angle and OH bond length) play an important role in the reaction path. However, a more detailed reaction coordinate analysis is required to better understand this aspect.[56]

For the trajectory which shows water elimination after ≈ 111 ps, see Figure 5B, several intramolecular H-transfers occur before $t = 108$ ps. In addition, large torsional and angular excursions are observed which leads to visiting both possible minimum energy structures, see Figure 3. Such motions occur on the picosecond time scale, as can be seen in Figure 5B. Concomitantly, the H5-O4-S1 angle and S1-O6 bond also pick up a considerable amount of energy which assists the eventual dissociation along coordinates H5-O4 and S1-O6.

3.3 Final State Analysis

Final state analysis is a meaningful way to characterize the outcome of a gas phase reaction. Because experimentally the direct investigation of the water elimination reaction is challenging, a computational exploration of the likely outcomes of such an experiment is potentially helpful. Contrary to previous efforts, the present simulations are capable of making concrete and quantitative statements about this aspect for several reasons. Firstly, MS-ARMD conserves total energy which is essential if a meaningful final state analysis is to be performed. Secondly, the current reactive PES is much improved over the previous force field in that it realistically captures the important torsional degrees of freedom. Thirdly, the present treatment allows both, intramolecular H-transfer and water elimination which is essential because the barrier height for both processes is similar.

In order to investigate the energy distribution after vibrational excitation and subsequent water elimination, the translational, rotational and vibrational energies in the reaction products were determined following established methodologies.[57] The analysis was carried out for all trajectories that experienced water elimination within 1 ns. The final state analysis starts when the sulfur-oxygen(water) distance exceeds 20 Å. Trajectories were then continued for an additional 5 ps during which 500 snapshots were collected and analyzed. Translational, rotational, vibrational, rovibrational energies and the rotational quantum number were computed for every snapshot and rotational and vibrational energies were averaged over all 500 snapshots from which probability distributions of the averaged values can be determined.

Figures 6 shows distributions for all energy components of the products for excitation of $\nu_9 = 5$ and 6, respectively. Three distributions, each normalized individually, are reported. One of them (solid line) is the overall distribution of the particular energy component which would be the expected experimental signal. The two histograms are distributions for direct water elimination (without prior intramolecular H-transfer) and energy distributions for events in which intramolecular H-transfer precedes water elimination, respectively. It is found that the two partial energy distributions peak at different maximal energies in general. This is most prominent for the translational and vibrational energies in SO_3. For $\nu_9 = 6$, a maximum peak at about 20 kcal/mol is observed for the H_2O-translational energy for the direct reaction, whereas for SO_3 this quantity peaks at 5 kcal/mol (Figure 6 grey trace). Contrary to that, reactions with prior H-transfer lead to a maximum peak in the translational energy distribution at 12 kcal/mol for H_2O and ≈ 3 kcal/mol in the case of SO_3. The translational energies of the products are correlated due to

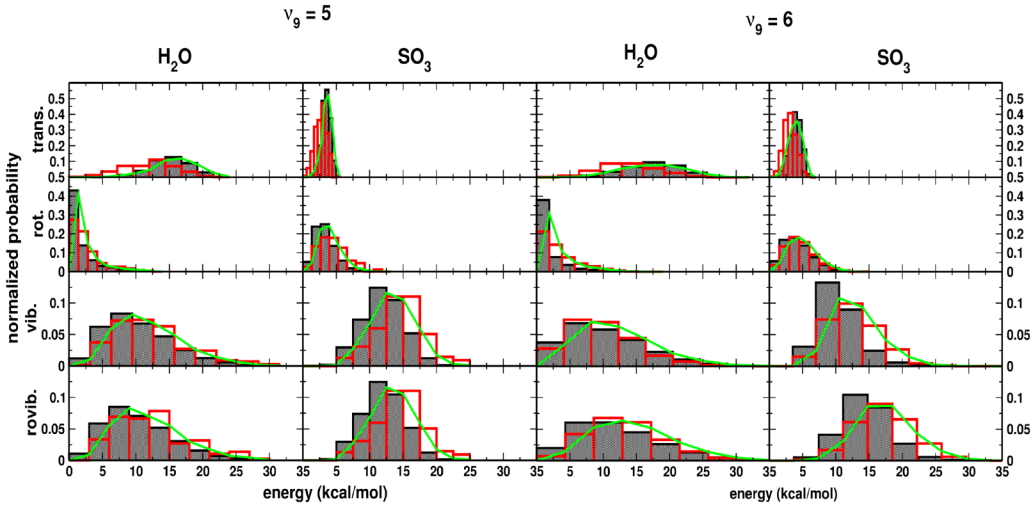

Fig. 6 Yosa et al.: Energy distribution for the H_2O and SO_3 fragments. Contribution of translational, rotational, vibrational and rovibrational energies are shown for the two processes; direct water elimination (black histograms) and water elimination preceded by intramolecular H-transfer (red histograms) for $\nu_9 = 5$ (left) and 6 (right). Overall distributions are represented by the green curve.

conservation of linear momentum, which was initially zero by preparation. On the other hand the rotational energies are similarly distributed for trajectories showing water elimination with or without previous H-transfer. The peaks for the two differ only by about 1 kcal/mol. The angular momenta of the products, and therefore their rotational energies, are not correlated, contrary to the linear momentum. This is due to the presence of orbital angular momentum.

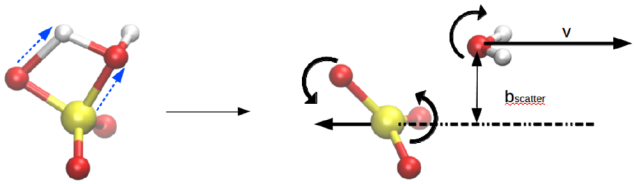

Fig. 7 Yosa et al.: Generation of the angular momenta in the final state. The blue arrows on H_2SO_4 illustrate the H-transfer step which leads to water elimination. Due to the off-center breakup and the conservation of total angular momentum the two fragments, SO_3 and H_2O, separate in a counterrotating manner with high fragment angular velocities, indicated by the curved arrows.

The angular momentum distributions can also be discussed within the framework of a scattering process. The geometrical situation is schematically summarized in Figure 7 where perpendicular distances of the asymptotic paths of the fragments are characterized by a Gaussian distribution centered around $b_{\mathrm{scatter}} \sim 0.7$Å. While the distributions for the direct and indirect mechanisms were distinctly different, they proved to be largely independent of the level of excitation: $b_{\mathrm{scatter}}^{\mathrm{direct}} = \mu \pm \sigma = 0.72 \pm 0.18$Å ($\nu_9 = 4$), 0.67 ± 0.19Å ($\nu_9 = 5$) and 0.66 ± 0.19Å ($\nu_9 = 6$) and $b_{\mathrm{scatter}}^{\mathrm{indirect}} = \mu \pm \sigma = 0.89 \pm 0.31$Å ($\nu_9 = 5$) and 0.85 ± 0.27Å ($\nu_9 = 6$). I.e. the impact parameter for direct water elimination is typically 25 % smaller than that for the indirect process. The magnitudes of b_{scatter} and the translational energies of the fragments explain the large orbital angular momentum ($L_{\mathrm{orbital}} \approx 60$). The high orbital angular momentum is compensated for by the rotational excitation of SO_3 (see Figure 8 panel B) to conserve the total angular momentum. This suggests that when the system slides down on the product side of the barrier the O-atom which looses its hydrogen atom will experience a significant force which is transmitted as a torque to the leaving SO_3 fragment. The relative magnitudes of the rotational excitation of the fragments ($j_{\mathrm{max}}^{(H_2O)} \sim 5$ vs. $j_{\mathrm{max}}^{(SO_3)} \sim 50$) can also be rationalized by noting that the rotational constants of H_2O and SO_3 differ by almost 2 orders of magnitude (9 to 27 cm^{-1} compared to 0.17 and 0.34 cm^{-1}, respectively)[58,59]. Noting that the two fragments receive similar amounts of rotational energy, the ratios of the maximum j follows from $B^{(H_2O)}/B^{(SO_3)} \sim 100 \sim (j_{\mathrm{max}}^{(SO_3)}/j_{\mathrm{max}}^{(H_2O)})^2$ from which one obtains $j_{\mathrm{max}}^{(SO_3)}/j_{\mathrm{max}}^{(H_2O)} \sim 10$ which is what is found in Figure 8.

Overall, the analysis suggests that when water elimination is preceded by H-transfer the excess energy goes into vibra-

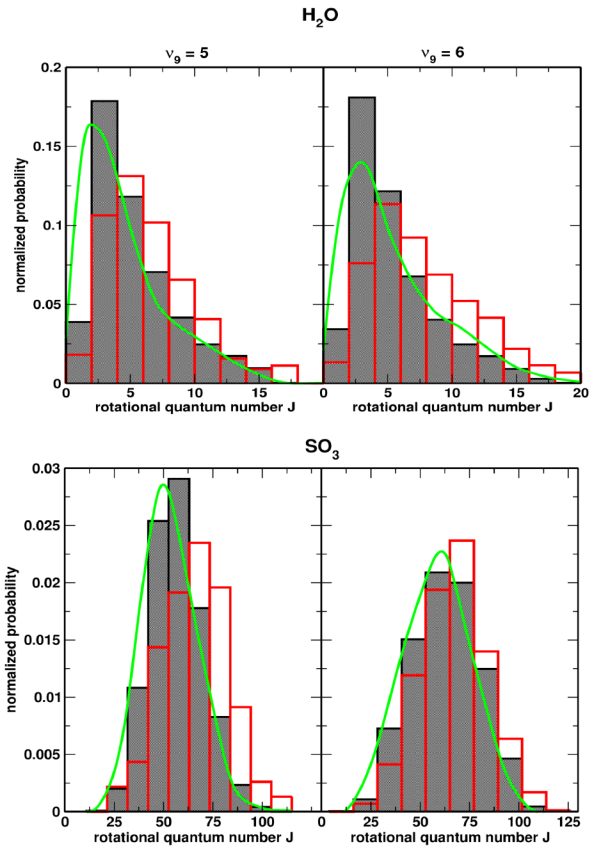

Fig. 8 Yosa et al.: Distribution of the H_2O and SO_3 rotational quantum numbers j for both, direct (black) and indirect (preceded intramolecular H-transfer) (red) water elimination for excitation of $\nu_9 = 5$ and 6. The overall distribution is the green curve

tional and rotational degrees of freedom. In other words, H-transfer during the nonequilibrium dynamics promotes energy redistribution within the complex. On the other hand, for direct water elimination the initial energy disposed in the system preferably goes into translational energy.

3.4 Kinetic analysis

Photoexcitation generates a non-equilibrium distribution of sulfuric acid molecules from the initial canonical ensemble at 300 K. Due to coupling between vibrational modes the ensemble relaxes to a microcanonical distribution at every energy if ergodicity for the undecayed species is assumed. However, because vibrational excitation to $\nu_9 \geq 4$ provides energy above the dissociation limit the available phase space can not be further explored by H_2SO_4 which limits the degree to which this system is ergodic. As the time scales for direct water elimination and IVR are similar, statistical rate theories which assume microcanonical or canonical ensembles, can not be employed.

In the following a simple kinetic model is set up to extract first-order rate parameters from the trajectories in order to characterize the long-time behavior of the system. The relaxation of the initially excited population of reactant molecules ($R_0^* = H_2SO_4^*(\nu_9 = 4,5,6)$) during the free dynamics is modeled as a process of n consecutive steps, including states R_i^* ($i = 1,\ldots,n$) which are relaxed to various extents. The final population (R_n^*) is considered to be fully relaxed which is a mixture of microcanonical ensembles with weights reflecting the initial canonical ensemble before excitation. Stepwise IVR to yield R_n^* (i.e. complete redistribution of the available energy) is related to the fact that under the present conditions (absence of a collision partner M), the deactivation process $R_n^* + M \rightarrow R_n + M$ can not occur. In other words, full relaxation is only possible if the time scales for IVR are shorter than the average collision time under atmospheric conditions. From each R_i^* the formation of excited (translationally, rotationally, vibrationally) products ($P^* = (H_2O + SO_3)^*$) is possible which is assumed to follow a first-order kinetics. Note that no distinction is made between products obtained from different reactant ensembles. The proposed kinetic model is the following:

$$R_0^* \xrightarrow{k_{\mathrm{IVR},0}} \ldots \xrightarrow{k_{\mathrm{IVR},i-1}} R_i^* \xrightarrow{k_{\mathrm{IVR},i}} \ldots \xrightarrow{k_{\mathrm{IVR},n-1}} R_n^* \qquad (4)$$

$$R_i^* \xrightarrow{k_i} P^* \quad i = 0,\ldots,n \qquad (5)$$

In the following it is assumed that a single rate coefficient, $k_{\mathrm{IVR},i}$ and k_i can characterize the average behavior of the various energy states in a given relaxation or decomposition step, respectively. This is a reasonable assumption as the average energy and its spread within the ensemble ($\bar{E}_{300\mathrm{K}} = 8.16$ kcal/mol and $\sigma_E = 2.27$ kcal/mol) are small compared to its average energy after excitation ≈ 47 kcal/mol or more). The decomposition rate from the fully relaxed ensemble can be considered as an approximation to the microcanonical rate coefficient at the particular average energy. The corresponding system of kinetic differential equations for the time-evolution of the probabilities for the various states is:

$$\frac{d[R_0^*]}{dt} = -(k_{IVR,0} + k_0)[R_0^*] \quad (6)$$

$$\frac{d[R_i^*]}{dt} = -(k_{IVR,i} + k_i)[R_i^*] + k_{IVR,i-1}[R_{i-1}^*] \qquad i = 1,...,n-1 \quad (7)$$

$$\frac{d[R_n^*]}{dt} = -k_n[R_n^*] + k_{IVR,n-1}[R_{n-1}^*] \quad (8)$$

$$\frac{d[P^*]}{dt} = \sum_{i=0}^{n} k_i[R_i^*] \quad (9)$$

Initially, the entire population (100%) is in R_0^* and the probability of all other R_i^* is zero: $[R_i^*](t=0) = 0$ for $i > 0$ and $P(t=0) = 0$. The product yield ($[P^*](t)/[R_0^*](t=0)$) as a function of time can be expressed in closed analytical form for a system of linear differential equations. Increasing the number of IVR steps (i.e. larger n) between the initial (R_0^*) and the fully relaxed ensembles (R_n^*) allows to more accurately describe the relaxation process. The solution of the kinetic differential equations were fitted to the results of the trajectory calculations for the first nanosecond with increasing n values, corresponding to increasingly detailed relaxation models. A good fit is obtained if the $\nu_9 = 4$ excitation relaxes with a single step ($n = 1$) whereas for excitations $\nu_9 = 5$ and 6 two and three-step relaxation models were required ($n = 2$ and $n = 3$), respectively.

It is noted that certain decomposition times, e.g. $\tau_n = 358$ ns for excitation of $\nu_9 = 4$, are considerably longer than the actual maximum simulation time. Consequently, it can not be excluded that longer atomistic simulations (which would be possible in principle by using MS-ARMD but less so with QM/MD) can lead to changes in these values. On the other hand, such a value follows the trend observed for higher excitations (e.g. for $\nu_9 = 6$) for which τ_n is about one order of magnitude longer than the next shorter decomposition time scale. Furthermore, the standard errors of the fitted parameters are typically around 1-2%, and always below 5%. Therefore the extrapolation of the kinetic curves and additional implications derived from them can be considered reliable, if one assumes that the kinetic model remains meaningful for longer timescales.

The need for additional relaxation steps to describe the observed kinetics for higher excitations is related to the fact that more energy has to be redistributed from a single mode, indicating that their R_0^* state is further from the fully equilibrated state. The first-order rate coefficients allow the definition of characteristic times $\tau = k^{-1}$ for the processes. The product yields and the fitted curves of the corresponding relaxation models are shown in Figure 9, and the fitted characteristic times are reported in Table 1.

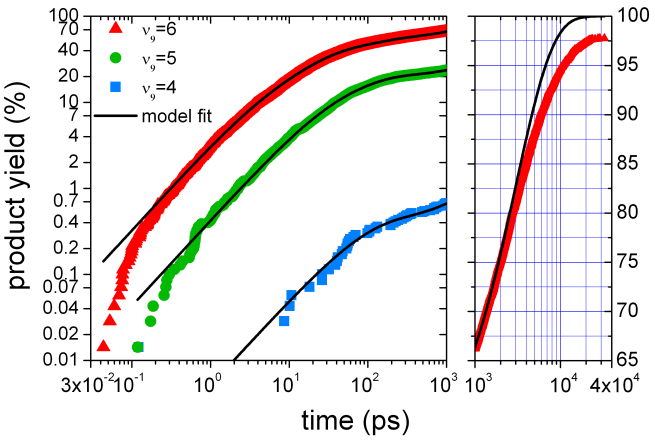

Fig. 9 Yosa et al.: Product yield as a function of time for the decomposition of sulfuric acid in free dynamics simulations after exciting the OH stretching vibrations with $\nu_9 = 4$, 5 and 6 quanta in a canonical ensemble of molecules at 300 K. A simple kinetic model (see text) was fitted to the data, which allows determination of characteristic times (see Table 1) for first order relaxation and decomposition processes (τ_{eq}) at the corresponding energies. Left panel reports data up to 1 ns with both axes on a logarithmic scale. The right panel (with yield on a linear scale) provides the data up to 40 ns which has only be determined for $\nu_9 = 6$. It is found that beyond ≈ 4 ns additional IVR time scales appear.

The general observation is that decomposition steps (τ_n) speed up with higher excitation and slow done with the progress of relaxation. This is in accord with the fact that a potential barrier has to be surpassed for the reaction to take place and the excitation of the OH stretching mode plays an important role in this. Decomposition from a non-relaxed ensemble (τ_{n-1}) is 1 to 2 orders of magnitude faster than decomposition from the relaxed ensembles (τ_n): 19.5 ns<360 ns ($\nu_9 = 4$), [233 ps, 680 ps] < 18.6 ns ($\nu_9 = 5$), and [30.6 ps, 64.0 ps, 403 ps] < 3 ns ($\nu_9 = 6$). In contrast to that, relaxation times for the IVR steps, τ_{IVR}, for all excitations are similar ($\tau_{IVR,n-1} = 80.7$ ps, 92.9 ps, 148 ps for $\nu_9 = 4$, 5 and 6 and $\tau_{IVR,n-2} = 23$ ps, 28.5 ps for $\nu_9 = 5$ and 6, respectively) This implies that the relaxation kinetics is less energy dependent the closer the ensemble is to its fully relaxed state.

Phenomenologically, this can be understood by considering the molecule as a system of coupled oscillators with well-defined coupling constants between them. The coupling parameters determine the relaxation time – i.e. the rate of energy exchange between various modes. With increasing energy content of individual vibrational modes higher order couplings become more important. Consequently, the relax-

ν_9	4	5	6	6′
E (kcal/mol)	46.8(±2.3)	55.4(±2.3)	63.5(±2.3)	
n	1	2	3	
$\tau_{\mathrm{IVR},n-3}$	-	-	3.9	5.2
$\tau_{\mathrm{IVR},n-2}$	-	23	28.5	33.7
$\tau_{\mathrm{IVR},n-1}$	80.7	92.9	148	145
τ_{n-3}	-	-	30.6	
τ_{n-2}	-	233	64.0	
τ_{n-1}	19500	680	403	
τ_n	358000	18600	3000	

Table 1 Yosa et al.: Number of IVR steps and corresponding relaxation ($\tau_{\mathrm{IVR},i}$) and decomposition (τ_i) times (in ps) for $\nu_9 = 4$, 5, and 6 inferred from the kinetic model by fitting to the trajectory data. For $\nu_9 = 6'$, no H-transfer was allowed during the simulation (see text) and only the IVR rate parameters were tuned, while other parameters were those from $\nu_9 = 6$. Relative fitting errors in the time scales τ are around 5 % at most. The average total energy and its standard deviation are reported for all ensembles.

ation timescales for the different excitations become similar as the ensembles get closer to their equilibrium.

For excitations $\nu_9 = 4$ and 5 the relaxation is significantly faster than decomposition from the initial non-equilibrium ensemble, which results in low conversion ($\approx 0.7\%$ and 24%) within 1 ns. For excitation of $\nu_9 = 6$ vibrational relaxation and direct decomposition have more similar rates, which leads to 66% conversion within 1 ns. Almost complete (i.e. 99% conversion) is expected within 1.6 μs, 80 ns and 11.6 ns for excitations of $\nu_9 = 4$, 5 and 6, respectively. As a comparison, the 40 ns trajectories with excitation of $\nu_9 = 6$ show conversion of 95.5 % within 11.6 ns after photoexcitation which compares with 99 % from the kinetic model (see right panel of Figure 9). Although the two approaches are in reasonable agreement with each other, the difference suggests that there is an additional process at longer times which can in fact be modelled if the number of relaxation steps is increased. However, whether or not such a process is relevant (and observable) depends on the environment. Under upper stratospheric-lower mesospheric conditions the deactivation of excited [$H_2SO_4^*$] molecules ($R_i^* \rightarrow R_i$) due to collisions with other molecules ("third bodies" (M)) need to be included:

$$R_i^* + M \xrightarrow{Z} R_i + M \quad i = 0, ..., n \tag{10}$$

where Z is the collision frequency. Assuming typical polar (75°S) conditions in the stratopause (at a height of 50 km) with a pressure $p \sim 70$ Pa, a temperature $T \sim 280$ K and a sum of the collision radii $r_{O_2/N_2} + r_{H_2SO_4} \sim 5$Å within the strong collision assumption (i.e. one collision is sufficient to deactivate the excited molecule), quenching occurs on the 130 ns timescale (inverse of the collision frequency, $\tau_{\mathrm{quench}} = (Z[M])^{-1}$), with quantum yields of approximately 30%, 90% and 99% for the 4, 5 and 6 excitation, respectively. This shows that the lowest ($\nu_9 = 4$) excitation cannot lead to full conversion in the ensemble due to quenching. Previous computational studies suggested integrated absorption cross sections of $2.0 \cdot 10^{-21}$, $1.9 \cdot 10^{-22}$, $2.6 \cdot 10^{-23}$ cm·molecule^{-1} for excitations with 4, 5 and 6 quanta, respectively.[16] They assumed unit photolysis quantum yields and concluded that the contribution of the highest excitation is negligible. Hence, first-order photolysis rate coefficients were considered only for excitations with 4 and 5 quanta. According to their calculations, the total photolysis rate coefficient varies only a little as a function of altitude due to slight changes in actinic flux with height.

From the lower mesosphere (70 km) downto lower altitudes in the stratosphere (20 km) the pressure and thereby the quenching rate increases by 1 to 3 orders of magnitude, which suggests that excitations with $\nu_9 = 5$ can dominate over $\nu_9 = 4$ and excitation into $\nu_9 = 6$ can also play a significant role in determining the photolysis rate at lower altitudes. In order to estimate the altitude-variation of the contribution of these excitations to the photolysis rates we carried out more rigorous calculations at various altitudes.

Considering pressures and temperatures typical in the relevant altitude range (see Figures 3.1 and 3.2 in reference[60]) at a latitude of 75°S (Antarctic), the photolysis quantum yields were calculated from the asymptotic ($t \rightarrow \infty$) solution of the kinetic model (Eq. 5) including quenching (Eq. 10). At this latitude the temperature varies non-monotonically between $200 - 280$ K within the altitude range of $20 - 70$ km, which results in a reduction by $0.55 - 2.72$ kcal/mol in the average thermal energies of sulfuric acid molecules compared to our simulations starting from thermalized sulfuric acid molecules at 300 K (8.16 ± 2.27 kcal/mol). This reduction is negligible compared to the average total vibrational energy of sulfuric acid molecules after photoexcitation (46.8, 55.4 and 63.4 kcal/mol, see Table 1). Therefore, the decomposition and relaxation lifetimes (τ_i) determined from fitting are good approximations for the relevant altitude range. The actinic flux in the investigated altitude and wavelength range (absorption lines at 741, 606 and 517 nm for $\nu_9 = 4, 5, 6$) varies only little with wavelength assuming clear sky conditions. Beside these assumptions, the photolysis quantum yields (Φ_i, where $i = \nu_9 = 4, 5, 6$) and fractional contributions (J_i / J_{total}) to the total photolysis rate are calculated for the altitude range of $20 - 70$ km (see Fig. 10). At these altitudes the characteristic quenching time will be comparable to the decomposition lifetime, which causes significantly reduced quantum yields for the lower excitations. Below 40 km photolysis via

excitation of the OH stretch with 5 quanta becomes dominant and at an altitude of 20 km excitations with 4 and 6 quanta will have a 20 % contribution to the photolysis rates (see Fig. 10 at 20 km $J_4/J_{\text{total}} = J_6/J_{\text{total}} = 20$ % and $J_5/J_{\text{total}} = 60\%$). Most importantly, the reduced quantum yields with excitation of $\nu_9 = 4$ and 5 in the stratosphere (below 50 km) cause significantly reduced photolysis rates compared to the case when quantum yields of 1 are assumed for all excitations. Due to quenching at a height of 70 km we predict a reduction of 14 % in total vibrationally induced photolysis rate coefficient. And this rate drops further due to even faster collisional quenching by a factor of 2.6 and 24 when descending to altitudes of 50 km and 20 km, respectively. Our calculations are an extension of and specification to the results of Vaida et al.[16] and show that a multi-level modeling is required to understand the significance of vibrationally induced decomposition pathways of sulfuric acid in the middle atmosphere.

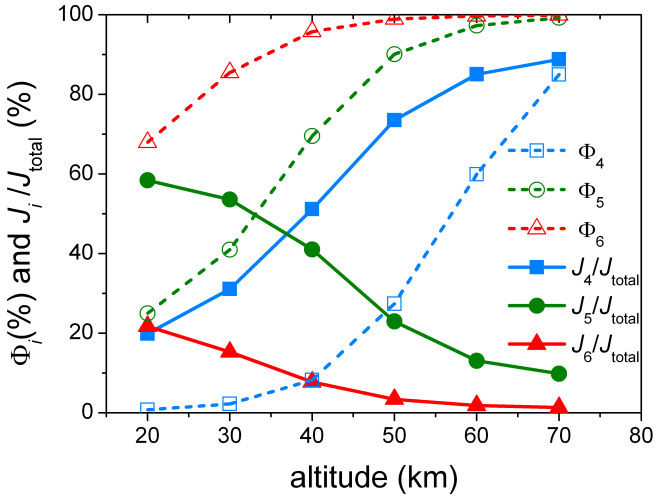

Fig. 10 After exciting OH-stretching vibrational mode with 4, 5 and 6 quanta in sulfuric acid, photolysis quantum yields (Φ_i) and fractional contributions (J_i/J_{total}) to the total photolysis rate (J_{total}) are shown are as a function of the altitude in the stratosphere and lower mesosphere.

In order to investigate the role of H-transfer in the IVR process, 1000 additional 300 ps trajectories were run for $\nu_9 = 6$ in which the H-transfer channel was closed. Hence, only one FF for H_2SO_4 and two for H_2O+SO_3 were used in the simulations. The same three-step kinetic model was fitted, but only the IVR timescales were allowed to vary while the water elimination parameters τ_n remained unchanged. An accurate fit was achieved with similar, small parameter variations (see column $\nu_9 = 6'$ in Table 1). The removal of H-transfer increased the timescales of first two IVR steps significantly, by 34% and 18%, which suggests that H-transfer plays a significant role in accelerating IVR.

4 Conclusions

In the present work it is demonstrated that rigorous reactive molecular dynamics simulations for small molecules in the gas phase can be used to characterize the final state distribution of photofragmentation processes. For the specific case of vibrationally induced photodissociation of H_2SO_4 to form H_2O and SO_3 the final state distributions will be useful in experimentally identifying such a reaction mechanism. Related work on Cl-CN following a more simplistic approach than the one pursued in the present work showed that a direct link between experiment and atomistic simulations can be established.[61,62] Contrary to previous simulations for water elimination in H_2SO_4 which were more qualitative in nature[30,32], the present work employs a refined and phyiscally more meaningful PES which allows to follow both, H-transfer and water elimination within the same framework. This is necessary because the two processes have similar barrier heights and can compete with each other. The results suggest that direct water elimination without preceding H-transfer follows exponentially decaying rate laws whereas the rate of the process proceeding through H-transfer is largely time-independent on the time scale of the present simulations (1 ns).

It is also interesting to compare the present results with earlier and more qualitative work.[30,32] Although a statistically significant number of reactive trajectories could be analyzed from the previous ARMD simulations, the computational model only allowed to follow one reaction channel, namely water elimination. This lead to quite different reaction time distributions compared to the present work which exhibits a more diverse and realistic reaction dynamics. Furthermore, the important torsional degrees of freedom are much more realistically represented in the current work but were only treated qualitatively in the earlier parametrization. The barriers for isomerization were much higher and therefore it was more difficult to transfer energy from the vibrationally excited OH stretching vibration into the torsions. Finally, the reaction barrier in the MS-ARMD PES is close to the best *ab initio* calculations but overestimated by several kcal/mol on the earlier PES. All these differences lead to modifications in the reaction time distributions. Nevertheless, the overall conclusion from the previous investigation, namely that vibrationally induced photodissociation is a relevant and probable decay mechanism for H_2SO_4 in the middle atmosphere, remains unchanged.

The kinetic model used to analyze the rates following excitation suggests that a one-step IVR relaxation process is sufficient to explain the data when exciting $\nu_9 = 4$ whereas an increasing number of relaxation steps is required for excitation of $\nu_9 \geq 5$. This is consistent a) with the fact that no water elimination with previous H-transfer has been observed (i.e. only direct water elimination) in the simulations with excitation of $\nu_9 = 4$ and b) with the fact that the barrier for water elimination (32.0 kcal/mol) is lower than that for H-transfer (36.6 kcal/mol). As for $\nu_9 = 4$ excitation occurs close to the barrier, this process may be influenced by the neglect of tunneling contributions. However, this does not affect the main conclusion of the present work, namely *that* vibrationally induced photodissociation is a viable route for decomposition of H_2SO_4 under the given circumstances.

A mechanistic interpretation of the various time scales in terms of elementary processes is not straightforward/evident. This is related to the fact that all elementary processes (H-transfer directly after excitation; subsequent H-transfers; water elimination) are characterized by distributions of reaction times and depending on the degree of relaxation, subsequent processes sensitively depend on the history of the trajectory. Including the possibility for third-body collisions and using realistic physical conditions for the relevant altitudes suggests that excitation of $\nu_9 = 5$ can become dominant for vibrationally induced photolysis below 40 km. For excitation by 4 quanta the quantum yield drops quickly with decreasing altitude, thereby excitation by 6 quanta can also become relevant for the photolysis rate in the lower stratosphere.

The present framework is a generic computational strategy to investigate non-RRKM decomposition reactions following vibrational excitation of small molecules in the gas phase. A challenging extension of the present work will consist of applying it to the reaction dynamics of excited molecules in solution. Several interesting experimental studies which provided fragmentation patterns following the excitation of small molecules in solution have recently appeared.[63,64] As the present and previous investigations have shown, simulations can provide a deeper understanding of energy migration pathways in such complex systems.[64,65]

References

1 R. Charlson, J. Lovelock, M. Andreae and S. Warren, *Nature*, 1987, **326**, 655 – 661.
2 R. Kiene, *Nature*, 1999, **402**, 363 – 368.
3 R. Sim and C. Pedrs-Ali, *Nature*, 1999, **402**, 396 – 399.
4 B. Huebert, *Nature*, 1999, **400**, 713 – 714.
5 K. Capaldo, J. Corbett, P. Kasibhatla, P. Fischbeck and S. Pandis, *Nature*, 1999, **400**, 743 – 746.
6 H. Niki, P. Maker, C. Savage and L. P. Breitenbach, *Int. J. Chem. Kinet.*, 1986, **15**, 743 – 746.
7 D. Grosjean, *Environ. Sci.*, 1984, **18**, 460 – 468.
8 R. Steudel, *Angew. Chem. Int. Ed.*, 1995, **34**, 1313 – 1315.
9 W.-K. Li and M. McKee, *J. Phys. Chem. A*, 1995, **101**, 9778 – 9782.
10 A. Kukui, V. Bossoutrot, G. Laverdet and G. Le Bras, *J. Phys. Chem. A*, 2000, **104**, 9935 – 946.
11 D. J. Hofmann and J. M. Rosen, *Nature*, 1982, **297**, 120–124.
12 F. Raes, R. V. Dingenen, E. Vignati, J. Wilson, J.-P. Pataud, J. H. Seinfeld and P. Adams, *Atmos. Environ. A-Gen.*, 2000, **34**, 4215 – 4240.
13 J. Rosen and D. Hofmann, *J. Geophys. Res.*, 1983, **88**, 3725 – 3731.
14 J. Burkholder, M. Mills and S. McKeen, *Geophys. Res. Lett.*, 2000, **27**, 2493 – 2496.
15 P. E. Hintze, H. G. Kjaergaard, V. Vaida and J. B. Burkholder, *J. Chem. Phys.*, 2003, **107**, 1112 – 1118.
16 V. Vaida, H. G. Kjaergaard, P. E. Hintze and D. J. Donaldson, *Science*, 2003, **299**, 1566 – 1568.
17 S. J. Wrenn, L. J. Butler, G. A. Rowland, C. J. Knox and L. F. Phillips, *J. Chem. Phys.*, 1999, **129**, 1112 – 1118.
18 H. G. Kjaergaard, J. R. Lane, A. L. Garden, D. P. Schofield, T. W. Robinson and M. Mills, *Adv. Quantum Chem.*, 2008, **55**, 1112 – 1118.
19 T. W. Robinson, D. P. Schofield and H. G. Kjaergaard, *J. Chem. Phys.*, 2003, **118**, 7226 – 7232.
20 J. R. Lane and H. G. Kjaergaard, *J. Phys. Chem. A*, 2008, **112**, 4958 – 4964.
21 J. Langmer, H. Rodhe, P. J. Crutzen and P. Zimmermann, *Nature*, 1992, **359**, 712 – 716.
22 D. Donaldson, G. J. Frost, K. H. Rosenlof and V. Tuck, A. F. Vaida, *Geophys. Res. Lett.*, 1997, **24**, 2651 – 2654.
23 V. Vaida and D. J. Donaldson, *Phys Chem Chem Phys.*, 2014, **16**, 827–836.
24 D. K. Havey, K. J. Feierabend and V. Vaida, *J. Mol. Struct-Teochem*, 2004, **680**, 243 – 247.
25 J. R. Lane, H. G. Kjaergaard, K. L. Plath and V. Vaida, *J. Phys. Chem. A*, 2007, **111**, 5434 – 5440.
26 P. E. Hintze, K. J. Feierabend, D. K. Havey and V. Vaida, *Spec. Acta A-Mol. Biomol. Spec.*, 2005, **61**, 559 – 566.
27 K. J. Feierabend, D. K. Havey, S. S. Brown and V. Vaida, *Chem. Phys. Lett.*, 2006, **420**, 438 – 442.
28 K. Morokuma and C. Muguruma, *J. Am. Chem. Soc.*, 1994, **116**, 10316 – 10317.
29 L. J. Larson, M. Kuno and F. M. Tao, *J. Chem. Phys.*, 2000, **112**, 8830 – 8838.
30 J. Yosa and M. Meuwly, *J. Phys. Chem. A*, 2011, **115**, 14350 – 14360.
31 R. D. Beck, P. Maroni, D. C. Papageorgopoulos, T. T. Dang, M. P. Schmid and T. R. Rizzo, *Science*, 2003, **302**, 98–100.
32 Y. Miller and R. B. Gerber, *J. Am. Chem. Soc.*, 2006, **128**, 9594 – 9595.
33 Y. Miller, R. B. Gerber and V. Vaida, *Geophys. Res. Lett.*, 2007, **34**, 1 – 5.
34 D. Blank, W. Sun, A. Suits, Y. Lee, S. North and G. Hall, *J. Chem. Phys.*, 1998, **108**, 5414–5425.
35 F. F. Crim, *Proc. Nat. Acad. Sci. USA*, 2008, **105**, 12654–12661.
36 M. P. Grubb, M. L. Warter, K. M. Johnson and S. W. North, *J. Phys. Chem. A*, 2011, **115**, 3218–3226.
37 T. Nagy, J. Yosa and M. Meuwly, *J. Chem. Theory. Comput.*, 2014, accepted.
38 D. R. Nutt and M. Meuwly, *Biophys. J.*, 2006, **90**, 1191–1201.
39 J. Danielsson and M. Meuwly, *J. Chem. Theory. Comput.*, 2008, **4**, 1083.
40 M. J. Frisch, G. W. Trucks, H. B. Schlegel, G. E. Scuseria, M. A. Robb, J. R. Cheeseman, J. A. J. Montgomery, T. Vreven, K. N. Kudin, J. C. Burant, J. M. Millam, S. S. Iyengar, J. Tomasi, V. Barone, B. Mennucci, M. Cossi, G. Scalmani, N. Rega, G. A. Petersson, H. Nakatsuji, M. Hada, M. Ehara, K. Toyota, R. Fukuda, J. Hasegawa, M. Ishida,

T. Nakajima, Y. Honda, O. Kitao, H. Nakai, M. Klene, X. Li, J. E. Knox, H. P. Hratchian, J. B. Cross, C. Adamo, J. Jaramillo, R. Gomperts, R. E. Stratmann, O. Yazyev, A. J. Austin, R. Cammi, C. Pomelli, J. W. Ochterski, P. Y. Ayala, K. Morokuma, G. A. Voth, P. Salvador, J. J. Dannenberg, V. G. Zakrzewski, S. Dapprich, A. D. Daniels, M. C. Strain, O. Farkas, D. K. Malick, A. D. Rabuck, K. Raghavachari, J. B. Foresman, J. V. Ortiz, Q. Cui, A. G. Baboul, S. Clifford, J. Cioslowski, B. B. Stefanov, G. Liu, A. Liashenko, P. Piskorz, I. Komaromi, R. L. Martin, D. J. Fox, T. Keith, M. A. Al-Laham, C. Y. Peng, A., M. Nanayakkara, P. M. W. Challacombe, B. Gill, Johnson, W. Chen, M. W. Wong, C. Gonzalez and J. A. Pople, *Gaussian 03, Revision C.01*, Gaussian, Inc., Wallingford CT, U.S.A., 2004.

41 G. Mie, *Ann. Phy.*, 1903, **316**, 657–697.

42 C. Breneman and K. Wiberg, *J. Chem. Comp.*, 1990, **11**, 361373.

43 A. MacKerell, D. Bashford, M. Bellott, R. Dunbrack, J. Evanseck, M. Field, S. Fischer, J. Gao, H. Guo, S. Ha, D. Joseph-McCarthy, L. Kuchnir, K. Kuczera, F. Lau, C. Mattos, S. Michnick, T. Ngo, D. Nguyen, B. Prodhom, W. Reiher, B. Roux, M. Schlenkrich, J. Smith, R. Stote, J. Straub, M. Watanabe, J. Wiorkiewicz-Kuczera, D. Yin and M. Karplus, *J. Phys. Chem. B*, 1998, **102**, 3586–3616.

44 J. Nelder and R. Mead, *Chem. Phys.*, 1965, **7**, 308 – 313.

45 T. Halgren and W. Lipscomb, *Chem. Phys. Lett.*, 1977, **49**, 225 – 232.

46 B. R. Brooks, C. L. Brooks, III, A. D. Mackerell, Jr., L. Nilsson, R. J. Petrella, B. Roux, Y. Won, G. Archontis, C. Bartels, S. Boresch, A. Caflisch, L. Caves, Q. Cui, A. R. Dinner, M. Feig, S. Fischer, J. Gao, M. Hodoscek, W. Im, K. Kuczera, T. Lazaridis, J. Ma, V. Ovchinnikov, E. Paci, R. W. Pastor, C. B. Post, J. Z. Pu, M. Schaefer, B. Tidor, R. M. Venable, H. L. Woodcock, X. Wu, W. Yang, D. M. York and M. Karplus, *J. Chem. Comp.*, 2009, **30**, 1545–1614.

47 M. Meuwly, A. Müller and S. Leutwyler, *Phys Chem Chem Phys.*, 2003, **5**, 2663–2672.

48 P. N. Nguyen and G. Stock, *J. Chem. Phys.*, 2003, **119**, 11350–11358.

49 J. Demaison, M. Herman, J. Lievin and H. D. Rudolph, *J. Phys. Chem. A*, 2007, **111**, 2602 – 2609.

50 L. Lohr, *J. Mol. Struct-Teochem*, 1982, **4**, 221 – 227.

51 Y. Zhao, B. J. Lynch and D. G. Truhlar, *J. Phys. Chem. A*, 2004, **108**, 4786–4791.

52 A. P. Scott and L. Radom, *The Journal of Physical Chemistry*, 1996, **100**, 16502–16513.

53 T. L. Tso and E. Lee, *J. Phys. Chem*, 1984, **88**, 2776–2781.

54 L. Schriver, D. Carrere, A. Schriver and K. Jaeger, *Chem. Phys. Lett.*, 1991, **181**, 505–511.

55 A. Givan, A. Larsen, A. Loewenschuss and C. Nielsen, *J. Mol. Str.*, 1999, **509**, 35–47.

56 A. Ma and A. Dinner, *J. Phys. Chem. B*, 2005, **109**, 6769–6779.

57 R. Schinke, *Annu. Rev. Phys. Chem.*, 1988, **39**, 39–68.

58 G. Herzberg, *Infrared and Raman Spectra*, Van Nostrand, Princeton, 1962.

59 V. Meyer, D. H. Sutter and H. Dreizler, *Z. Naturforsc. A.*, 1991, **46**, 710–714.

60 G. P. Brasseur and S. Solomon, *Aeronomy ofthe Middle Atmosphere*, Springer, P.O.Box 17,3300 AA Dordrecht,The Netherlands., 2005.

61 S. Lutz and M. Meuwly, *ChemPhysChem*, 2012, **13**, 305–313.

62 S. A. Barts and J. B. Halpern, *J. Phys. Chem.*, 1989, **93**, 7346 – 7351.

63 A. C. Crowther, S. L. Carrier, T. J. Preston and F. F. Crim, *J. Phys. Chem. A*, 2009, **113**, 3758–3764.

64 C. A. Rivera, N. Winter, R. V. Harper, I. Benjamin and S. E. Bradforth, *Phys Chem Chem Phys.*, 2011, **13**, 8269 – 8283.

65 M. W. Lee and M. Meuwly, *J. Phys. Chem. A*, 2011, **115**, 5053–5061.